Observing topological phase transition in ferromagnetic transition metal dichalcogenides

Shilei Ji [●], Ruijia Yao, Chuye Quan, and Yile Wang

Institute of Advanced Materials (IAM), Nanjing University of Posts and Telecommunications (NJUPT), Nanjing 210023, China

Jianping Yang

School of Science, Nanjing University of Posts and Telecommunications (NJUPT), Nanjing 210023, China

Xing'ao Li [●][*]

School of Science, Nanjing University of Posts and Telecommunications (NJUPT), Nanjing 210023, China
and College of Science, Zhejiang University of Science and Technology, Hangzhou 310023, China

Two-dimensional transition metal dichalcogenides (TMDs) are considered a suitable platform to study topological properties such as the quantum anomalous Hall effect. However, this quantum transport property is usually found in systems with a small band gap. For large-band-gap TMDs, the nature of quantum transport is difficult to find. In this work, with the analysis of the $k \cdot p$ model, we investigate the topological phases of ferromagnetic TMDs in the cases of a large gap and small gap. By analyzing the orbital Berry curvature, we reveal that the orbital Hall effect in the system possesses a nontrivial topological invariant $C_L = -1$ when $\text{sgn}(\Delta_{+1}\Delta_{-1}) > 0$, where Δ_τ represents the band gap at the τ valley (K or K' valley). Consequently, the large-gap ferromagnetic TMDs exhibit properties of an orbital Hall insulator. In the case of $\text{sgn}(\Delta_{+1}\Delta_{-1}) < 0$, we demonstrate that the small-gap system transforms into a quantum anomalous Hall insulator with a Chern number $C = 1$. Both topological phases are valley polarized and robust in the presence of an out-of-plane magnetic moment. Subsequently, we illustrate this transition from an orbital Hall insulator to a quantum anomalous Hall insulator in FeCl$_2$, a representative ferromagnetic TMD, by tuning the Coulomb correction U_{eff} to manipulate the valley band gaps.

I. INTRODUCTION

Two-dimensional (2D) transition metal dichalcogenides (TMDs), like MoS$_2$, possess intriguing spin-indegenerate valleys located at the six vertices of their first Brillouin zone [1–5]. The absence of spatial inversion symmetry in TMDs leads to interesting consequences for electron movement in these valleys [6–10]. The Berry curvature (BC) comes into play, influencing the trajectories of electrons in different energy valleys and giving rise to charge accumulation that is perpendicular to the direction of current injection. In recent years, TMDs have emerged as an ideal platform for investigating a wide range of Hall effects due to their unique electronic and topological properties [11–14]. Among these Hall effects, the anomalous Hall effect (AHE) is particularly fascinating as it is coupled to the valley degree of freedom in the absence of a magnetic field [12,15–17]. The intrinsic AHE can be detected in the system with the time inversion symmetry broken, such as ferromagnetic TMDs [12,18–20]. Moreover, in previous work, we induce the AHE in nonmagnetic TMD by the Janus method. The clean and specific valley model makes TMDs suitable for studying AHE [21].

As the band gaps of 2D TMDs close, the electronic states at the K and K' valleys become topologically nontrivial, leading to the emergence of the quantum anomalous Hall effect (QAHE) [14,17,22,23]. In this state, the electronic states at the edge of the material become chiral, conducting without scattering, and carrying a quantized Hall conductance. In addition, the quantization of the Hall conductance is directly related to the Chern number, an integer topological invariant that characterizes the nontrivial topology of the band structure. Zhou *et al.* have induced QAHE coupled with valley index in ferromagnetic honeycomb lattices [16]. The quantized Hall conductance was observed in the K valley, with the Chern number $C = C_K = -1$. Recently, Hu *et al.* found the intrinsic QAHE in the half-valley-metal FeCl$_2$, which results from the spin-orbital coupling (SOC) effect and large exchange interaction of the d orbital in transition metals [24]. The chiral edge state connecting the conduction valley and valence valley is topologically protected in the insulating gap. However, as the insulating gap gradually opens, QAHE is absent in the ferromagnetic TMDs, making them topologically trivial [14,17,22,23]. Another question then arises: Are ferromagnetic TMDs with large band gap topologically trivial, or can there be quantized Hall conductance that can be detected in the large band gap?

Here we focus on the orbital Hall effect (OHE), which gives rise to a current with the orbital angular momentum

---

(OAM) perpendicular to the applied in-plane electric field [25–27]. Contrary to the AHE, the OHE does not require the SOC effect. Interestingly, OHE has been used to explain the origin of the huge AHE in some materials [28]. Furthermore, the theoretical calculations predict the existence of a significant orbital Hall conductance (OHC) with nonzero orbital Chern number in monolayer (1L) and bilayer (2L) nonmagnetic MoS_2 [7].

Inspired by the above works, we expand the application of OHE to ferromagnetic TMDs, and discuss the topological properties in it. The two-band $k \cdot p$ model of ferromagnetic TMDs is constructed to analyze the transport properties at the valleys. It is found that the sign of the orbital Berry curvature (OBC) and BC is related to the sign of Δ_τ, where Δ_τ represents the band gap at the τ valley and $\tau = +1\,(-1)$ is the $K\,(K')$ valley. We consider two regimes: (1) sgn $(\Delta_{+1}\Delta_{-1}) > 0$ and (2) sgn$(\Delta_{+1}\Delta_{-1}) < 0$. In the first regime, the band gap opens at two valleys. We find that the system is an orbital Hall (OH) insulator with the orbital Chern number $C_L = -1$. Meanwhile, the AHE cannot be observed within the band gap. In the second regime, the gap at one of the valleys closes and reopens, causing the sign of Δ_τ to be reversible. We show that the current system is a quantum anomalous Hall (QAH) insulator with the Chern number $C = 1$. Due to the opposite sign of the OBC, the OHE is absent in this case with $C_L = 0$. Based on the result of the $k \cdot p$ model, we use a ferromagnetic $FeCl_2$ as a prominent example to investigate the topological phase transition between an OH insulator and a QAH insulator.

II. $k \cdot p$ MODEL FOR ORBITAL HALL EFFECT

Traditional ferromagnetic TMD monolayers, such as H-VSe_2, breaking the spatial and time-reversal symmetry at the same time, have a space group of D_{3h} [8]. The unique and clean valley model at the K and K' points has been investigated in the fields of electrical, optical, and magnetic transport [8,29–31]. Based on the space group and valley model at TMD monolayers, we construct a two-band $k \cdot p$ model with the exchange interaction to describe the OAM transport near the $K\,(K')$ valley. The basis function of the valance state and the conduction state at the $K\,(K')$ valley is

$$\psi_v^\tau = \frac{|d_{x^2-y^2}\rangle + i\tau |d_{xy}\rangle}{\sqrt{2}}, \tag{1a}$$

$$\psi_c^\tau = |d_{z^2}\rangle. \tag{1b}$$

The index $\tau = +1\,(-1)$ represents the $K\,(K')$ valley, and v/c denotes the valence/conduction state. Considering the SOC term H_{SOC} and exchange interaction term H_{ex}, the effective Hamiltonian H_{eff} can be written as below,

$$H_{eff} = \hat{s}_0 H_0 + H_{soc} + H_{ex}, \tag{2a}$$

$$H_0 = I\epsilon + \frac{\Delta}{2}\hat{\sigma}_z + v_F(\tau\hat{\sigma}_x k_x + \hat{\sigma}_y k_y), \tag{2b}$$

$$H_{soc} = \tau\hat{s}_z(\lambda_c\hat{\sigma}_+ + \lambda_v\hat{\sigma}_-), \tag{2c}$$

$$H_{ex} = -\hat{s}_z(m_c\hat{\sigma}_+ + m_v\hat{\sigma}_-). \tag{2d}$$

Here, v_F is the massless Fermi velocity of the Dirac electrons, and $\hat{\sigma}_i$ and $\hat{s}_i$ $(i = 0, x, y, z)$ are Pauli matrices for pseudospin

and spin, respectively. ϵ indicates the on-site energy introduced in order to set the Fermi level at zero, and I is the identity matrix. $\lambda_v\,(\lambda_c)$ is the SOC parameter for the valence (conduction) band. $m_v\,(m_c)$ denotes the effective exchange splitting of the valence (conduction) band. $\hat{\sigma}_\pm$ is defined as $\frac{1}{2}(\hat{\sigma}_0 \pm \hat{\sigma}_z)$.

When considering the exchange splitting, the spin channels at the top of the valence band for both K and K' valleys are spin-down. The spin index is -1, and the Hamiltonian eigenvalues are expressed as

$$E_\pm = \frac{1}{2}\big(E_0 \pm \sqrt{4v_F^2 k^2 + \Delta_\tau^2}\big). \tag{3}$$

In Eq. (3), we use $E_0 = \epsilon - \tau(\lambda_c + \lambda_v) + (m_c + m_v)$ and $\Delta_\tau = \Delta - \tau(\lambda_c - \lambda_v) + (m_c - m_v)$, respectively. In addition, k^2 is equal to $k_x^2 + k_y^2$. Once constructing the effective Hamiltonian of ferromagnetic TMD monolayers, we can calculate the Berry curvature at the valley $\Omega_{n,xy}^{z,\tau}(\boldsymbol{k})$ and relevant Hall conductance by the Kubo formula [32],

$$\Omega_{n,xy}^{z,\tau}(\boldsymbol{k}) = -2\hbar^2 \sum_{n\neq n'} \frac{\text{Im}\langle\psi_{nk}|\hat{v}_x|\psi_{n'k}\rangle\langle\psi_{n'k}|\hat{v}_y|\psi_{nk}\rangle}{(E_{n'} - E_n)^2}, \tag{4}$$

where $\hat{v}_i$ $(i = x, y)$ is the velocity operator along the k_i direction, with $\hat{v}_i = \frac{1}{\hbar}\frac{\partial H}{\partial k_i}$. Here we use the eigenvalues of Eq. (2) to calculate $\Omega_{n,xy}^z(\boldsymbol{k})$, and the corresponding eigenstates are given by

$$|\psi_+\rangle = [\tau D_k^+, D_k^- e^{-i\tau\phi}]^T, \tag{5a}$$

$$|\psi_-\rangle = [D_k^-, -\tau D_k^+ e^{-i\tau\phi}]^T, \tag{5b}$$

where $D_k^\pm = \sqrt{\frac{1}{2} \pm \frac{\Delta_\tau}{2E}}$, $E = \sqrt{4v_F^2 k^2 + \Delta_\tau^2}$, and $\phi = \tan^{-1}(k_y/k_x)$. The BC at the τ valley for the valance band can be simplified as

$$\Omega_{n,xy}^{z,\tau}(\boldsymbol{k}) = -\frac{2\tau v_F^2 \Delta_\tau}{\big(4v_F^2 k^2 + \Delta_\tau^2\big)^{3/2}}. \tag{6}$$

It turns out that the sign of the BC is related to the valley index τ and gap Δ_τ. $\Omega_{n,xy}^{z,\tau}(\boldsymbol{k})$ has the same sign on both valleys only if the symbols of Δ_τ are opposite on both valleys. When the K point moves away from the valley, the BC disappears. Thus, the total BC $\Omega_{n,xy}^z(\boldsymbol{k})$ for the valence band can be regard as the sum of $\Omega_{n,xy}^{z,\tau}(\boldsymbol{k})$.

In addition, the OBC can be calculated using [26,33]

$$\Omega_{n,xy}^{z,\tau,\text{orb}}(\boldsymbol{k}) = -2\hbar \sum_{n\neq n'} \frac{\text{Im}\langle\psi_{nk}|\hat{J}_x|\psi_{n'k}\rangle\langle\psi_{n'k}|\hat{v}_y|\psi_{nk}\rangle}{(E_{n'} - E_n)^2}. \tag{7}$$

Compared to Eq. (4), the $\hat{v}_x$ is replaced with $\hat{J}_x$, where, the OAM operator $\hat{J}_x$ is defined as $\hat{J}_x = \frac{1}{2}(\hat{v}_x\hat{L}_z + \hat{L}_z\hat{v}_x)$. $\hat{L}_z$ is the z component of the OAM operator. In the $k \cdot p$ model, based on the basis function of ψ_c^τ and ψ_v^τ defined in Eq. (11), the OAM operator can be chosen as $\hat{L}_z = \text{diag}(0, 2\hbar\tau)$ for analytical solution of OHE. The OBC at special valley can be simplified as

$$\Omega_{n,xy}^{z,\tau,\text{orb}}(\boldsymbol{k}) = -\frac{2v_F^2 \Delta_\tau}{\big(4v_F^2 k^2 + \Delta_\tau^2\big)^{3/2}} = \tau \times \Omega_{n,xy}^{z,\tau}. \tag{8}$$

It is found that, for the valance band, a large $|\Omega_{v,xy}^{z,\tau,\text{orb}}(\boldsymbol{k})|$ exists at two valleys $(k \to 0)$, and the sign is independent of the
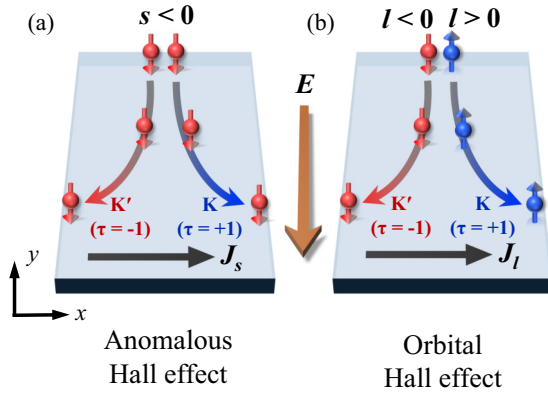
FIG. 1. Illustration of (a) anomalous Hall effect and (b) orbital Hall effect. The ball with arrow represents the carrier with spin angular momentum s in (a) and orbital angular momentum l in (b), respectively. The red and blue color of the ball is the direction of corresponding angular momentum. By applying an electronic field E along y axis, the flow of carriers depends on the valley index τ in anomalous Hall insulator and l in orbital Hall insulator, respectively.

valley index. Compared to $\Omega_{v,xy}^{z,\tau}(\boldsymbol{k})$, $\Omega_{v,xy}^{z,\tau,\mathrm{orb}}(\boldsymbol{k})$ has opposite sign at the K' valley ($\tau = -1$).

The orbital Chern number which can characterize the topologically nontrival phases can be expressed with the momentum sum of the corresponding BC,

$$
\begin{aligned}
C_L &= \frac{1}{2\pi} \int_{\mathrm{BZ}} \sum_{\tau} \Omega_{v,xy}^{z,\tau,\mathrm{orb}}(\boldsymbol{k}) d^2k \\
&= \frac{1}{2\pi} \sum_{\tau} \int_{\mathrm{BZ}} -\frac{2v_F^2 \Delta_\tau}{\left(4v_F^2 k^2 + \Delta_\tau^2\right)^{3/2}} d^2k \\
&= -\frac{1}{2}[\mathrm{sgn}(\Delta_{+1}) + \mathrm{sgn}(\Delta_{-1})].
\end{aligned} \tag{9}
$$

In addition, the Chern number can be written as $C = -\frac{1}{2}[\mathrm{sgn}(\Delta_{+1}) - \mathrm{sgn}(\Delta_{-1})]$. At the same time, the corresponding Hall conductance σ_{xy} of the Hamiltonian in Eq. (2) is related to the Chern number,

$$
\sigma_{xy}^{\mathrm{AH}} = -\frac{e^2}{h}C, \quad \sigma_{xy}^{\mathrm{OH}} = -\frac{e}{2\pi}C_L. \tag{10}
$$

The schematic representation of the AHE $\sigma_{xy}^{\mathrm{AH}}$ and the OHE $\sigma_{xy}^{\mathrm{OH}}$ is depicted in Fig. 1, and we will discuss the phenomena in Sec. III C. Note that the nontrivial topology is related to the gap Δ_τ at two valleys. When the case $\mathrm{sgn}(\Delta_{+1}\Delta_{-1}) > 0$ is satisfied, only integer multiples of the OH signal exist with $C_L = -1$. The system is an OH insulator. On the other hand, when the signs of the two Δ_τ are opposite $[\mathrm{sgn}(\Delta_{+1}\Delta_{-1}) < 0]$, the system reveals integer multiples of the anomalous Hall (AH) signal with $C = 1$, which is a QAH insulator. Therefore, as the gap at valleys changes, the topology phase transition can be observed at 2D TMDs.

III. DFT RESULTS AND DISCUSSION

A. Methods

First-principles calculations are performed within the frame of density functional theory (DFT) using the Vienna

Ab initio Simulation Package (VASP) based on the projected augmented wave (PAW) method [34–36]. The electron configurations of the Fe and Cl atoms are $4s^2 3d^6$ and $3s^2 3p^5$, respectively. The plane-wave cutoff energy is set to 500 eV and a k-point grid of $15 \times 15 \times 1$ is used. The force on each atom is smaller than 1 meV Å^{-1}. A vacuum space of greater than 15 Å is inserted along the $+Z$ axis to avoid the interaction between adjacent layers. The weak van der Waals interaction considered in 1L $FeCl_2$ is described by the DFT-D3 method [37]. The SOC effect is considered in the nonstatic self-consistent calculations. The magnetic anisotropy energy (MAE) calculation is defined as $E_{100} - E_{001}$, where a positive (negative) value indicates that the easy magnetization axis is interlayer (intralayer). The Coulomb correction U_{eff} with the Dudarev method has been applied to manipulate the electronic structure of $FeCl_2$ [38].

In addition, the mostly localized Wannier functions including the d orbital of the Fe atom and p orbital of the Cl atom are constructed on a denser k mesh of $301 \times 301 \times 1$ for the 1L $FeCl_2$ by using the WANNIER90 package [32,39–42]. The anomalous and OH conductance as well as their corresponding BC are computed by a modified version of the Wanniertools program [43]. In the OH conductance calculation, the matrix representations of $|p_y\rangle$, $|p_z\rangle$, $|p_x\rangle$, and $|d_{xy}\rangle$, $|d_{yz}\rangle$, $|d_{z^2}\rangle$, $|d_{xz}\rangle$, $|d_{x^2-y^2}\rangle$ are

$$
\hat{L}_z^p = \hbar \begin{pmatrix} 0 & 0 & -i \\ 0 & 0 & 0 \\ i & 0 & 0 \end{pmatrix}, \quad \hat{L}_z^d = \hbar \begin{pmatrix} 0 & 0 & 0 & 0 & 2i \\ 0 & 0 & 0 & i & 0 \\ 0 & 0 & 0 & 0 & 0 \\ 0 & -i & 0 & 0 & 0 \\ -2i & 0 & 0 & 0 & 0 \end{pmatrix}. \tag{11}
$$

B. Atomic and electronic structure of $FeCl_2$

To investigate the possibility of a topology phase transition in H-$FeCl_2$, a ferrovalley material, we examine its atomic structure, which is displayed in Fig. 2(a). Similar to H-VSe_2, H-$FeCl_2$ has a hexagonal honeycomb crystal structure with vertical mirror symmetry, described by the space group D_{3h} [8,24]. From the side view, each magnetic atomic layer of Fe atoms is sandwiched by a single atomic layer of Cl atoms. Fe atoms are covalently bonded by the six nearest-neighboring Cl atoms to form trigonal prismatic coordination with the bond length $r = 2.47$ Å. This gives rise to a local crystal field on each Fe atom with the $3d$ orbitals splitting into the A_1' orbital (d_{z^2}), E' orbital ($d_{xy}, d_{x^2-y^2}$), and E'' orbital (d_{xz}, d_{yz}) as illustrated in Fig. 2(b). Considering that there are 6 electrons in the outermost $3d$ orbital, the spin-up electron channels in $FeCl_2$ are fully occupied, while the remaining electron occupies the spin-down A_1 orbital. Consequently, each Fe atom possesses a magnetic moment of $4\mu_B$. Furthermore, the bond angle $\theta = 86°$ of Fe-Cl-Fe demonstrates that the long-range magnetic order on $FeCl_2$ comes from superexchange interactions between Fe-Cl-Fe.

Out-of-plane magnetic anisotropy (MA) is crucial for maintaining long-range magnetic order in 2D ferromagnetic materials [14,44,45]. The Mermin-Wagner theory predicts that in the absence of out-of-plane MA, 2D magnetic systems with continuous symmetry will not exhibit genuine long-range
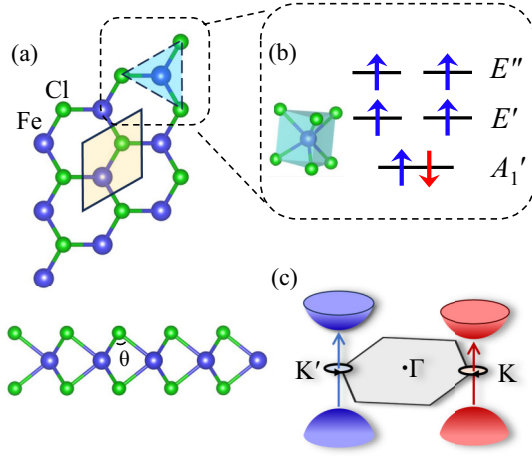
FIG. 2. The atomic structure of 1L FeCl$_2$. (a) The top view and the side view of FeCl$_2$. (b) Splitting of the $3d$ orbitals of Fe atom into A_1' orbital (d_{z^2}), E' orbital (d_{xy}, $d_{x^2-y^2}$), and E'' orbital (d_{xz}, d_{yz}) in a trigonal prismatic crystal field. (c) The first Brillouin zone and inequivalent valley of FeCl$_2$.

TABLE I. Fitting results from DFT band structure calculations. The unit is eV for U_{eff}, ϵ, Δ, v_F, m_v, m_c, λ_v, and λ_c.

U_{eff}	ϵ	Δ	v_F	m_v/m_c	λ_v/λ_c	C_L/C
0.00	−2.47	0.43	1.25	1.23/1.20	−0.05/0.00	−1/0
1.16	−2.86	0.11	1.29	1.46/1.40	−0.03/−0.03	0/1

magnetic ordering at finite temperatures [46]. This is because thermal fluctuations strongly impact the orientation of spins in a 2D system, preventing the long-range order from emerging. However, out-of-plane MA hinders the influence of thermal fluctuations on the orientation of magnetic spins, thus preserving the magnetic exchange interaction between neighboring magnetic moments. Therefore, under specific conditions of out-of-plane MA, the 2D magnetic system can display genuine long-range magnetic order at finite temperatures. In this work, our primary focus is on the out-of-plane MA of FeCl$_2$. The detailed out-of-plane MA is depicted in Fig. 3(a) (see also

Table I). It can be observed that for 1L FeCl$_2$, the out-of-plane MA occurs at smaller values of parameter U_{eff}. When U_{eff} is larger than 1.16 eV, the magnetic moments in FeCl$_2$ tend to orient within the xy plane. Therefore, our main investigation revolves around the electronic structure and transport properties of FeCl$_2$ in the range of U_{eff} from 0 to 1.16 eV.

Due to the hexagonal honeycomb structure and broken spatial inversion symmetry, TMD materials like FeCl$_2$ exhibit inequivalent valley polarization at the K and K' points in the presence of out-of-plane MA. The detailed band gaps are summarized in Fig. 3(b). At small values of parameter U_{eff} (0.00–1.10 eV), the band gap at the valley opens up, resulting in a valley polarization of 110 meV in FeCl$_2$. The band structure at the valley of FeCl$_2$ is mainly contributed by the E' and A_1' orbitals, respectively, which determine the valence band maximum and conduction band minimum when the valley band gap is open [taking $U_{eff} = 0.00$ eV as an example in Fig. 3(c)]. Using Eq. (1) as the basis function, we constructed a model for the valley polarization splitting [21]:

$$\Delta E_v = i\langle d_{x^2-y^2}|H_{soc}|d_{xy}\rangle - i\langle d_{xy}|H_{soc}|d_{x^2-y^2}\rangle$$
$$= 2|\lambda_v|\cos\theta,$$
$$\Delta E_c = i\langle d_{z^2}|H_{soc}|d_{z^2}\rangle - i\langle d_{z^2}|H_{soc}|d_{z^2}\rangle$$
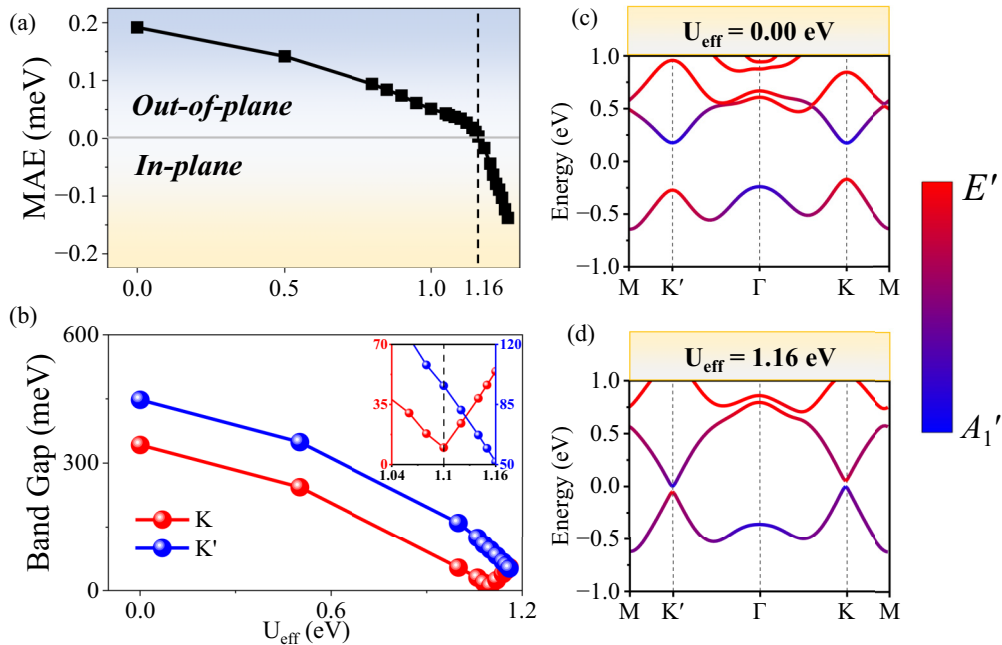$$= 0, \tag{12}$$

FIG. 3. The electronic structure of 1L FeCl$_2$. (a) The magnetic anisotropy and (b) the band gap of FeCl$_2$, where red and blue balls represent the band gaps at K and K' valleys. (c), (d) The band structure at $U_{eff} = 0.00$ eV and $U_{eff} = 1.16$ eV. As is shown in the figure, the main contribution at the valleys is A_1' and E' orbitals.
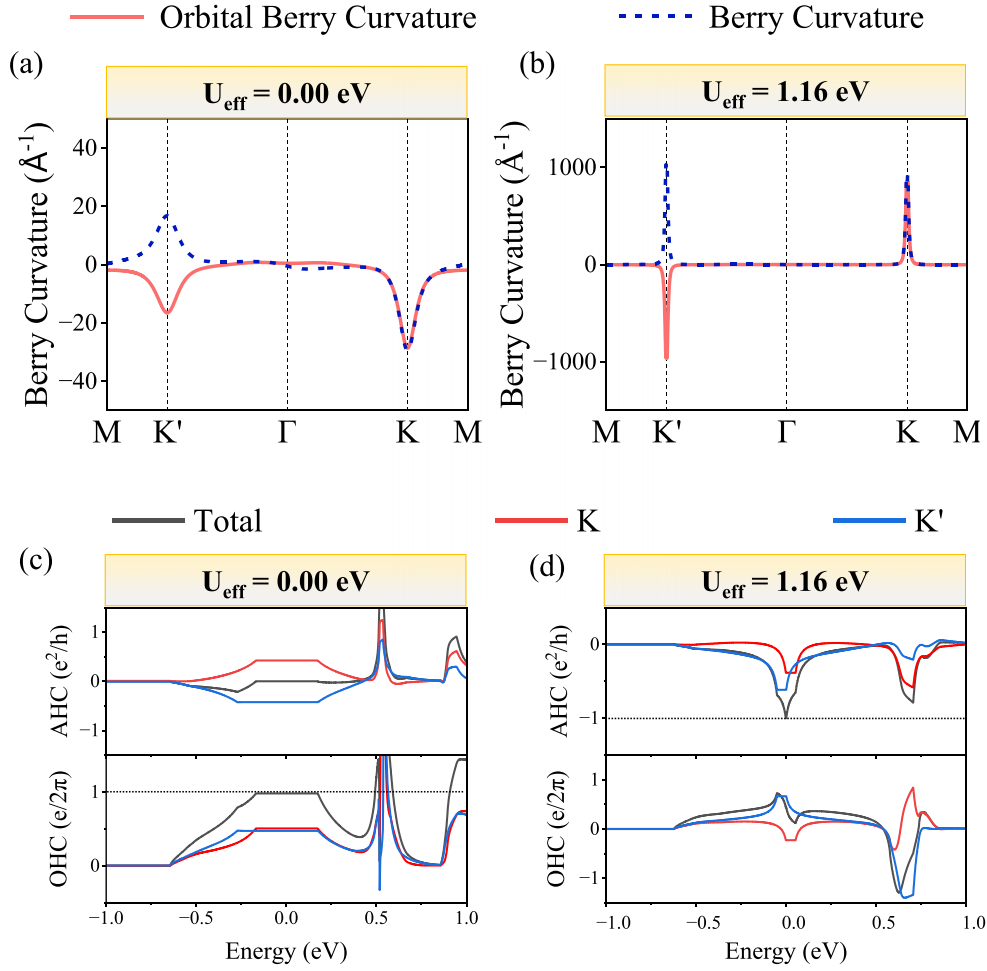
FIG. 4. The orbital Berry curvature (red) and Berry curvature (blue) with (a) $U_{eff} = 0.00$ eV, (b) $U_{eff} = 0.00$ eV. The anomalous Hall conductance (AHC) and the orbital Hall conductance (OHC) with (c) $U_{eff} = 0.00$ eV, (d) $U_{eff} = 1.16$ eV. Up and down panels are AHC and OHC, respectively. Black, red, and blue lines represent the corresponding Hall conductance at the total Brillouin zone, K valley, and K' valley.

where ΔE_v and ΔE_c denote valley polarization at the valance and conduction bands, respectively. The spin-polarized angle $\theta = 0°$ represents the magnetic moment along the Z axis. It is found that valley polarization arises from a combination of intrinsic SOC effect and spin polarization. When the magnetic moment flips, the band gaps of two valleys exchange with each other. Furthermore, when the value of parameter U_{eff} reaches 1.10 eV, the band at the K valley exhibits a closure, leading FeCl$_2$ to undergo a transition into a half-valley-metal (HVM) state. It is noteworthy that within the range of U_{eff} values between 1.10 eV and 1.16 eV, the band gap at the K valley reopens, but there is a change in the orbital contributions. In this case, the conduction band minimum (CBM) is mainly contributed by the E' orbital, while the valence band maximum (VBM) is predominantly contributed by the A'_1 orbital. Consequently, we consider the band gap at the K valley to have a negative value after the orbital contributions undergo a flip or reversal in this case.

Indeed, the changes in the Coulomb correction lead to two distinct states in FeCl$_2$. The first state, denoted as sgn($\Delta_{+1}\Delta_{-1}$) > 0, corresponds to the situation where the band gaps at both K and K' valleys open simultaneously. The second state, referred to as sgn($\Delta_{+1}\Delta_{-1}$) < 0, occurs when

the band gap at the K valley closes and then reopens with a negative value. These two states align with the two scenarios discussed in Sec. II.

C. Orbital and anomalous Hall signal in FeCl$_2$

In solids, the BC describes the phase evolution of electrons in momentum space within electronic bands [17,47,48]. Nonzero BC can give rise to AHE in the system breaking time-reversal symmetry, which is an essential electrical measurement technique used to probe the transport properties of ferromagnetic materials. In an AHE device, as illustrated in Fig. 1(a), the injected currents moving along the y axis experience an effect influenced by nonzero BC, resulting in a Lorentz force parallel to the x axis. This force causes the carriers to accumulate at the two ends of the device along the x axis, generating the AH signal. In this study, based on the two electronic structure states mentioned in Sec. III B ($U_{eff} = 0.00$ eV and $U_{eff} = 1.16$ eV), we have computed both the BC and the OBC by using Eqs. (4) and (7), which are plotted in Fig. 4. The OBC and BC around valleys can be written as $\Omega_{xy}^{z,\tau,orb}(k) = -\frac{2v_F^2\Delta_\tau}{(4v_F^2k^2+\Delta_\tau^2)^{3/2}} = \tau \times \Omega_{xy}^{z,\tau}$. At the valleys, the magnitudes of OBC and BC are related to

the band gap Δ_τ. Therefore, we consider two cases, (1) $\mathrm{sgn}(\Delta_{+1}\Delta_{-1}) > 0$ and (2) $\mathrm{sgn}(\Delta_{+1}\Delta_{-1}) < 0$, which represent $U_{\mathrm{eff}} = 0.00$ eV and 1.16 eV, respectively.

For the first case of $\mathrm{sgn}(\Delta_{+1}\Delta_{-1}) > 0$ in Figs. 4(a) and 4(c), the signs of Δ_τ at both valleys are the same, which leads to the same sign of OBC at two valleys. Meanwhile, the BC has opposite sign, as the coefficient of τ compared to OBC. By integrating the whole BC and OBC through the Brillouin zone, the anomalous Hall conductance (AHC) $\sigma_{xy}^{\mathrm{AH}}$ and OHC $\sigma_{xy}^{\mathrm{OH}}$ can be obtained [32],

$$\sigma_{xy}^{\mathrm{AH}} = -\frac{e^2}{\hbar} \int_{\mathrm{BZ}} \frac{d^2k}{(2\pi)^2} \Omega_{xy}^z(\boldsymbol{k}),$$

$$\sigma_{xy}^{\mathrm{OH}} = -\frac{e^2}{\hbar} \int_{\mathrm{BZ}} \frac{d^2k}{(2\pi)^2} \Omega_{xy}^{z,\mathrm{orb}}(\boldsymbol{k}). \tag{13}$$

The detailed calculation results are presented in Fig. 4(c). For a large-gap system ($U_{\mathrm{eff}} = 0.00$ eV), the AHC at the K and K' valleys exhibits opposite signs, which results in the inability to detect the AH signal in the valley of $FeCl_2$. The sign of the BC is related to the direction of the Lorentz force experienced by carriers in the AHE device. When carriers experience BC with opposite signs at the two valleys, they will move in opposite directions at the two valleys. As a result, the accumulation of carriers at the two ends of the AHE device along the x axis becomes equal, leading to the disappearance of the AH signal.

In addition, the OHC in this case is different from AHC due to the valley-independent OBC. It is clear that compared to zero AHC, the OHC at $U_{\mathrm{eff}} = 0.00$ eV is equal to $-C_L \frac{e}{2\pi}$, with the orbital Chern number $C_L = -1$. According to the definition of QAHE, we believe that this integer multiple of the OHC is a quantum transport property, which has a robust nonzero orbital Chern number. Equation (8) supports the notion that the OBC is gap dependent and has the same symbol in the case of $\mathrm{sgn}(\Delta_{+1}\Delta_{-1}) > 0$. This means the carriers with the opposite OAM at the two valleys are subject to the Lorentz force in the opposite direction in $FeCl_2$, thus accumulating on the two sides to form current with OAM. Consequently, the large-gap $FeCl_2$ is an OH insulator with the topological invariant $C_L = -1$.

In the case of $\mathrm{sgn}(\Delta_{+1}\Delta_{-1}) < 0$ in Figs. 4(b) and 4(d), the band gaps Δ_τ at the valleys have opposite signs, which leads to the same sign of the BC at both valleys. It is found that the small-gap $FeCl_2$ is a QAH insulator with integer multiples AHC in the Fermi level. The bulk of this system is insulated, while the edge state behaves as a unidirectional current without the band gap. At the same time, compared to $U_{\mathrm{eff}} = 0.00$ eV, the OBC changes the sign at K valleys, resulting in the negative contribution of OHC in Fig. 4(d). Consequently, the total OHC is greatly smaller than $1 \times \frac{e}{2\pi}$. In the case of $\mathrm{sgn}(\Delta_{+1}\Delta_{-1}) < 0$, $FeCl_2$ becomes another topological state, the QAHE with Chern number $C = 1$. The topological phase diagram of the Chern number and orbital Chern number is calculated with varied U_{eff} in Fig. 5. For a large-gap ferromagnetic TMD, there is an OH insulator. As
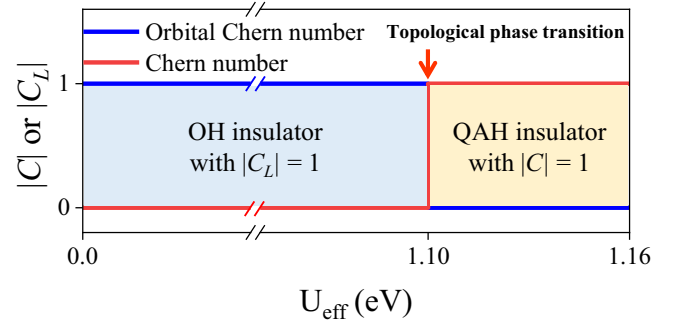

FIG. 5. Topological phase diagram of $FeCl_2$ with varied U_{eff}.

the band gap gradually decreases to 0 eV, the system switches to another topological state QAHE. Experimentally, through the magneto-optical Kerr effect, the accumulation of orbital magnetic moments is directly detected on the surface of light metal Ti [25]. We believe that this method is also suitable for the OHE measurement of 2D TMDs, and that 2D ferromagnetic TMDs are suitable platforms for studying the OHE and QAHE.

IV. CONCLUSION

In summary, we demonstrate the OH insulator for the large-gap ferromagnetic TMDs and the QAH insulator for the small-gap system. For the case of $\mathrm{sgn}(\Delta_{+1}\Delta_{-1}) > 0$, the large-gap ferromagnetic TMDs have robust orbital magnetic moments and accumulate perpendicular to the electric field through OBC, forming an OH insulator. The same sign of the OBC at two valleys leads to orbital Chern number $C_L = -1$. For the case of $\mathrm{sgn}(\Delta_{+1}\Delta_{-1}) < 0$, the ferromagnetic TMDs switch to QAH insulator with quantized Chern number $C = 1$. The OHE and QAHE are valley polarized and robust at the out-of-plane MA. As a result, two topological states were found on the magnetic TMDs. When the band gap is large, there is an OHE with $C_L = -1$ in the system; when the band gap gradually closes, there is a QAHE with $C = 1$ in the system. Taking a traditional TMD material $FeCl_2$ as an example, we observe the topological phase transition between an OH insulator and a QAH insulator. We remark that OHE with $C_L = -1$ occurs mainly in large-gap TMDs, which excludes QAHE interference. In addition, the intrinsic SOC for the $3d$ transition metal is weak, so in the insulating band gap, the influence of the spin Hall effect can also be excluded. Therefore, 2D TMDs are a very suitable platform for studying OH insulators. In addition, it is feasible to observe the topological phase transition from an OH insulator to a QAH insulator by interfacial engineering.

[1] M. Deng, X. Wang, J. Chen, Z. Li, M. Xue, Z. Zhou, F. Lin, X. Zhu, and Z. Fang, Plasmonic modulation of valleytronic emission in two-dimensional transition metal dichalcogenides, Adv. Funct. Mater. **31**, 2010234 (2021).

[2] S. Li, W. Wu, X. Feng, S. Guan, W. Feng, Y. Yao, and S. A. Yang, Valley-dependent properties of monolayer $MoSi_2N_4$, WSi_2N_4, and $MoSi_2As_4$, Phys. Rev. B **102**, 235435 (2020).

[3] X. Liu, A. P. Pyatakov, and W. Ren, Magnetoelectric coupling in multiferroic bilayer VS_2, Phys. Rev. Lett. **125**, 247601 (2020).

[4] D. Xiao, G. B. Liu, W. Feng, X. Xu, and W. Yao, Coupled spin and valley physics in monolayers of MoS_2 and other group-VI dichalcogenides, Phys. Rev. Lett. **108**, 196802 (2012).

[5] J. Zhou, J. Lin, H. Sims, C. Jiang, C. Cong, J. A. Brehm, Z. Zhang, L. Niu, Y. Chen, Y. Zhou, Y. Wang, F. Liu, C. Zhu, T. Yu, K. Suenaga, R. Mishra, S. T. Pantelides, Z. G. Zhu, W. Gao, Z. Liu *et al.*, Synthesis of Co-doped MoS_2 monolayers with enhanced valley splitting, Adv. Mater. **32**, 1906536 (2020).

[6] M. Costa, B. Focassio, L. M. Canonico, T. P. Cysne, G. R. Schleder, R. B. Muniz, A. Fazzio, and T. G. Rappoport, Connecting higher-order topology with the orbital Hall effect in monolayers of transition metal dichalcogenides, Phys. Rev. Lett. **130**, 116204 (2023).

[7] T. P. Cysne, M. Costa, L. M. Canonico, M. B. Nardelli, R. B. Muniz, and T. G. Rappoport, Disentangling orbital and valley Hall effects in bilayers of transition metal dichalcogenides, Phys. Rev. Lett. **126**, 056601 (2021).

[8] W. Y. Tong, S. J. Gong, X. Wan, and C. G. Duan, Concepts of ferrovalley material and anomalous valley Hall effect, Nat. Commun. **7**, 13612 (2016).

[9] D. Xiao, W. Yao, and Q. Niu, Valley-contrasting physics in graphene: Magnetic moment and topological transport, Phys. Rev. Lett. **99**, 236809 (2007).

[10] Q.-Q. Zhang, Q. Li, X.-T. An, and J.-J. Liu, Valley-resolved quantum anomalous Hall effect in ferromagnetically proximitized monolayer $MoTe_2$, Phys. Rev. B **105**, 205436 (2022).

[11] S. Bhowal and S. Satpathy, Intrinsic orbital and spin Hall effects in monolayer transition metal dichalcogenides, Phys. Rev. B **102**, 035409 (2020).

[12] X. Feng, X. Xu, Z. He, R. Peng, Y. Dai, B. Huang, and Y. Ma, Valley-related multiple Hall effect in monolayer VSi_2P_4, Phys. Rev. B **104**, 075421 (2021).

[13] Z. He, R. Peng, Y. Dai, B. Huang, and Y. Ma, Single-layer ScI_2: A paradigm for valley-related multiple Hall effect, Appl. Phys. Lett. **119**, 243102 (2021).

[14] W. Pan, Tuning the magnetic anisotropy and topological phase with electronic correlation in single-layer H-$FeBr_2$, Phys. Rev. B **106**, 125122 (2022).

[15] W. Y. Tong and C. G. Duan, Electrical control of the anomalous valley Hall effect in antiferrovalley bilayers, npj Quantum Mater. **2**, 47 (2017).

[16] J. Zhou, Q. Sun, and P. Jena, Valley-polarized quantum anomalous Hall effect in ferrimagnetic honeycomb lattices, Phys. Rev. Lett. **119**, 046403 (2017).

[17] X. Zhou, R.-W. Zhang, Z. Zhang, W. Feng, Y. Mokrousov, and Y. Yao, Sign-reversible valley-dependent Berry phase effects in 2D valley-half-semiconductors, npj Comput. Mater. **7**, 160 (2021).

[18] Y. Ma, Y. Wu, J. Tong, L. Deng, X. Yin, L. Zhou, X. Han, F. Tian, and X. Zhang, Distinct ferrovalley characteristics of

[19] the Janus RuClX (X = F, Br) monolayer, Nanoscale **15**, 8278 (2023).

[19] T. Zhang, X. Xu, B. Huang, Y. Dai, and Y. Ma, 2D spontaneous valley polarization from inversion symmetric single-layer lattices, npj Comput. Mater. **8**, 64 (2022).

[20] P. Zhao, Y. Liang, Y. Ma, and T. Frauenheim, Valley physics and anomalous valley Hall effect in single-layer h-MNX (M = Ti, Zr, Hf; X = Cl, Br), Phys. Rev. B **107**, 035416 (2023).

[21] S. Ji, R. Yao, C. Quan, J. Yang, F. Caruso, and X. Li, Anomalous valley Hall effect induced by mirror symmetry breaking in transition metal dichalcogenides, Phys. Rev. B **107**, 174434 (2023).

[22] H. Huan, Y. Xue, B. Zhao, G. Gao, H. Bao, and Z. Yang, Strain-induced half-valley metals and topological phase transitions in MBr_2 monolayers (M = Ru, Os), Phys. Rev. B **104**, 165427 (2021).

[23] S. Li, Q. Wang, C. Zhang, P. Guo, and S. A. Yang, Correlation-driven topological and valley states in monolayer VSi_2P_4, Phys. Rev. B **104**, 085149 (2021).

[24] H. Hu, W.-Y. Tong, Y.-H. Shen, X. Wan, and C.-G. Duan, Concepts of the half-valley-metal and quantum anomalous valley Hall effect, npj Comput. Mater. **6**, 129 (2020).

[25] Y. G. Choi, D. Jo, K. H. Ko, D. Go, K. H. Kim, H. G. Park, C. Kim, B. C. Min, G. M. Choi, and H. W. Lee, Observation of the orbital Hall effect in a light metal Ti, Nature (London) **619**, 52 (2023).

[26] D. Go, D. Jo, C. Kim, and H. W. Lee, Intrinsic spin and orbital Hall effects from orbital texture, Phys. Rev. Lett. **121**, 086602 (2018).

[27] D. Jo, D. Go, and H.-W. Lee, Gigantic intrinsic orbital Hall effects in weakly spin-orbit coupled metals, Phys. Rev. B **98**, 214405 (2018).

[28] H. Kontani, T. Tanaka, D. S. Hirashima, K. Yamada, and J. Inoue, Giant orbital Hall effect in transition metals: Origin of large spin and anomalous Hall effects, Phys. Rev. Lett. **102**, 016601 (2009).

[29] J. Liu, W. J. Hou, C. Cheng, H. X. Fu, J. T. Sun, and S. Meng, Intrinsic valley polarization of magnetic VSe_2 monolayers, J. Phys.: Condens. Matter **29**, 255501 (2017).

[30] C. B. Luo, X. Y. Peng, J. F. Qu, and J. X. Zhong, Valley degree of freedom in ferromagnetic Janus monolayer H-VSSe and the asymmetry-based tuning of the valleytronic properties, Phys. Rev. B **101**, 245416 (2020).

[31] C. Shen, G. Wang, T. Wang, C. Xia, and J. Li, Spin orientation and strain tuning valley polarization with magneto-optic Kerr effects in ferrovalley VS_2 monolayer, Appl. Phys. Lett. **117**, 042406 (2020).

[32] D. J. Thouless, M. Kohmoto, M. P. Nightingale, and M. denNijs, Quantized Hall conductance in a two-dimensional periodic potential, Phys. Rev. Lett. **49**, 405 (1982).

[33] S. Bhowal and S. Satpathy, Intrinsic orbital moment and prediction of a large orbital Hall effect in two-dimensional transition metal dichalcogenides, Phys. Rev. B **101**, 121112(R) (2020).

[34] P. E. Blochl, Projector augmented-wave method, Phys. Rev. B **50**, 17953 (1994).

[35] G. Kresse and J. Furthmuller, Efficient iterative schemes for *ab initio* total-energy calculations using a plane-wave basis set, Phys. Rev. B **54**, 11169 (1996).

[36] G. Kresse and D. Joubert, From ultrasoft pseudopotentials to the projector augmented-wave method, Phys. Rev. B **59**, 1758 (1999).

[37] S. Grimme, J. Antony, S. Ehrlich, and H. Krieg, A consistent and accurate *ab initio* parametrization of density functional dispersion correction (DFT-D) for the 94 elements H-Pu, J. Chem. Phys. **132**, 154104 (2010).

[38] A. Rohrbach, J. Hafner, and G. Kresse, Electronic correlation effects in transition-metal sulfides, J. Phys.: Condens. Matter **15**, 979 (2003).

[39] T. Jungwirth, Q. Niu, and A. H. MacDonald, Anomalous Hall effect in ferromagnetic semiconductors, Phys. Rev. Lett. **88**, 207208 (2002).

[40] A. A. Mostofi, J. R. Yates, Y. S. Lee, I. Souza, D. Vanderbilt, and N. Marzari, wannier90: A tool for obtaining maximally-localised Wannier functions, Comput. Phys. Commun. **178**, 685 (2008).

[41] X. Wang, J. R. Yates, I. Souza, and D. Vanderbilt, *Ab initio* calculation of the anomalous Hall conductivity by Wannier interpolation, Phys. Rev. B **74**, 195118 (2006).

[42] Y. Yao, L. Kleinman, A. H. MacDonald, J. Sinova, T. Jungwirth, D. S. Wang, E. Wang, and Q. Niu, First principles calculation of anomalous Hall conductivity in ferromagnetic bcc Fe, Phys. Rev. Lett. **92**, 037204 (2004).

[43] Q. Wu, S. Zhang, H.-F. Song, M. Troyer, and A. A. Soluyanov, WannierTools: An open-source software package for novel topological materials, Comput. Phys. Commun. **224**, 405 (2018).

[44] S. D. Guo, X. S. Guo, G. Z. Wang, K. Cheng, and Y. S. Ang, Electric-field induced magnetic-anisotropy transformation to achieve spontaneous valley polarization, J. Mater. Chem. C **10**, 16363 (2022).

[45] S. Zhang, R. Xu, N. Luo, and X. Zou, Two-dimensional magnetic materials: Structures, properties and external controls, Nanoscale **13**, 1398 (2021).

[46] C. Gong and X. Zhang, Two-dimensional magnetic crystals and emergent heterostructure devices, Science **363**, eaav4450 (2019).

[47] Y. Wang, W. Wei, H. Wang, N. Mao, F. Li, B. Huang, and Y. Dai, Janus TiXY monolayers with tunable Berry curvature, J. Phys. Chem. Lett. **10**, 7426 (2019).

[48] D. Xiao, M.-C. Chang, and Q. Niu, Berry phase effects on electronic properties, Rev. Mod. Phys. **82**, 1959 (2010).